ELSEVIER

Journal of Marine Systems 18 (1998) 115–134

JOURNAL OF MARINE SYSTEMS

Efficient ocean modeling using non-hydrostatic algorithms

John Marshall *, Helen Jones, Christopher Hill

Department of Earth, Atmospheric and Planetary Sciences, Massachusetts Institute of Technology, Cambridge, USA

Received 8 March 1996; accepted 16 June 1997

Abstract

A solution strategy for the incompressible Navier Stokes equations (INS) is outlined, which renders ocean models based on them competitive with those that assume hydrostatic balance on all scales. It is shown that non-hydrostatic models rooted in INS can be designed which, when deployed in the hydrostatic limit, require no more computational effort than models based on the hydrostatic primitive equations (HPE). But unlike HPE, the model can also be used to address convective, non-hydrostatic scales if its resolution is increased. The ideas are illustrated in simulations of convection, baroclinic instability and large-scale circulation in the Mediterranean.

Keywords: ocean modeling; non-hydrostatic algorithms; Navier Stokes equations

1. Introduction

In this paper, we consider some algorithmic aspects of ocean models rooted in the incompressible Navier Stokes equations (hereafter INS). Such models do not a priori make the hydrostatic approximation and so permit study of small-scale convective processes, as well as large-scale motions. Conventional ocean models employ approximated forms of the Navier Stokes equations, using numerical schemes based on the 'hydrostatic primitive equations' (or HPEs), in which the vertical momentum equation is reduced to a statement of hydrostatic balance and the 'traditional approximation' is made, in which the Coriolis force is treated approximately and the shallow atmosphere approximation is made. On a large-scale, the HPEs omit terms that are generally thought to be small, but on small scales, such as those associated with the convective scale, the scaling assumptions implicit in them become increasingly problematic. Indeed, to model convective dynamics in the ocean, one must use models based on INS.

It is a widely held belief that models based on INS are not suited to studying and simulating large-scale processes because of the computational overhead inherent in INS algorithms. In this paper, however, we describe a solution method for INS which, because it is sensitive to the transition from non-hydrostatic to hydrostatic dynamics, can also perform competitively with hydrostatic models in the hydrostatic limit. First, in Section 2, we discuss the hydrostatic approximation and its breakdown, identifying the relevant non-dimensional numbers. Insight gained from this analysis informs our numerical strategy, in

* Corresponding author.

0924-7963/98/$ - see front matter
PII: S0924-7963(98)00008-6

which the pressure field is separated into surface, hydrostatic and non-hydrostatic parts. In Section 3, the approach is illustrated in numerical studies of the interplay between convective (unbalanced) and baroclinically unstable (balanced) motions. In Section 4, the method is applied to model the general circulation of the entire Mediterranean basin, showing that there is no overhead in using INS rather than a more traditional HPE model. Complete details of the numerical methods and physical rationale behind the modeling strategy can be found in Marshall et al. (1997a,b). Programming issues are discussed in Shaw et al. (1998), which compares data parallel to implicitly parallel programming paradigms.

2. Models of hydrostatic and non-hydrostatic dynamics

Consider the schematic diagrams sketched in Fig. 1 showing the convective deepening of a mixed layer in the ocean. In Fig. 1a, an initially resting stratified fluid is subject to widespread and uniform buoyancy loss from the surface; the layer deepens by drawing buoyancy from depth through convection that exchanges parcels of fluid in the vertical. Such convection, occurring on scales of perhaps 1 km or less in the ocean, is fundamentally non-hydrostatic. Suppose now, however, as in Fig. 1b, that spatial inhomogeneities (in buoyancy forcing or ambient stratification) induce lateral gradients in mixed-layer depth and density. Now the mode of buoyancy transfer through the mixed layer can change from a non-hydrostatic convective one, to a hydrostatically balanced motion in which fluid parcels are exchanged laterally on slanting paths in baroclinic instability. The baroclinic instability scale is a few kilometers in the oceanic mixed layer. This switch, from predominantly non-hydrostatic to hydrostatic motion, will be illustrated by numerical experiment in Section 3.

Models that assume hydrostatic balance a priori cannot, for example, be used to study the interplay between convection and baroclinic instability depicted in Fig. 1. Let us now inquire into the range of applicability of hydrostatic models by identifying the scale on which the hydrostatic approximation breaks down, and how it depends on external parameters.

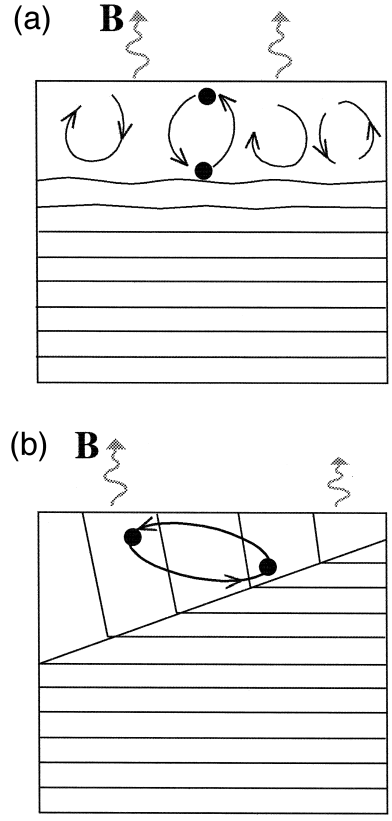

Fig. 1. (a) A schematic diagram showing convection triggered by buoyancy loss at the surface of an initially resting stratified fluid. We imagine that the buoyancy loss is constant in time and spatially uniform. Upright convection develops in response, drawing buoyancy from depth to balance loss from the surface. (b) Now, if large-scale lateral density gradients are induced by spatial variations in the surface buoyancy loss (or equally, spatial variations in the N^2 of the underlying fluid), the mode of buoyancy transfer through the convective layer can change from a (non-hydrostatic) convective one to a hydrostatically balanced motion in which fluid parcels are exchanged on slanting paths in baroclinic instability.

2.1. The hydrostatic approximation

We discuss the transition from INS to hydrostatically/geostrophically balanced dynamics by considering the balance of terms in the governing equations. In so doing, we will identify the relevant non-dimensional parameters; in particular, a non-hydrostatic parameter n, which is a measure of the ratio of the magnitude of non-hydrostatic to hydrostatic pressures. This suggests, and leads to, a solu-

tion strategy for INS which, in the hydrostatic limit, is as economical as those based on HPE. Unlike HPE, however, INS asymptotes to the unapproximated equations as the resolution of the model increases.

Identifying and exploiting the transition from unbalanced, non-hydrostatic motion to hydrostatic, geostrophic, dynamics is essential if an efficient algorithm is to be designed. Accordingly, in Appendix A, we non-dimensionalize INS and consider the balance of terms if the flow is close to one of hydrostatic and geostrophic balance. There are three important non-dimensional numbers: The Rossby number, $R_o = U/fL$, a measure of rotation effects, the Richardson number, $R_i = N^2h^2/U^2$, a measure of the strength of the stratification and $\gamma = h/L$, a measure of the aspect ratio of the motion. Quasi-geostrophic dynamics occur at large R_i and small R_o, such that $R_i R_o^2 \simeq 1$ (that is on the Rossby-radius scale Nh/f).

The non-dimensional form of the momentum, continuity and thermodynamic equations may be written in terms of R_0, R_i and γ thus (see Appendix A) [1]

$$R_o \frac{D'\mathbf{v}'_\mathbf{h}}{Dt'} + \left(\nabla'_h(p'_s + p'_{hy} + nqp'_{nh}\right) + f'\mathbf{k}\times\mathbf{v}'_\mathbf{h}\Big) = 0 \quad (1)$$

$$\frac{D'w'}{Dt'} + \frac{\partial p'_{nh}}{\partial z'} = 0 \quad (2)$$

$$\frac{D'b'}{Dt'} + N'^2 w' = 0 \quad (3)$$

$$R_o \frac{\partial w'}{\partial z'} + \nabla'_h \cdot \mathbf{v}'_\mathbf{h} = 0 \quad (4)$$

where D/Dt is the total derivative, $v = (v_h, w)$ is the velocity, b is the buoyancy, f is the Coriolis parameter, z is the height, p is the pressure, ∇_h is the horizontal divergence operator and N^2 is the Brunt–Vaissala frequency. In the above, primed variables are non-dimensional and assumed to be of order unity.

[1] Here the Cartesian form of INS is analyzed, in which only Coriolis terms depending on $2\Omega\sin$(latitude) are retained; the role of $2\Omega\cos$(latitude) terms which are neglected in HPE are discussed in Marshall et al. (1997a).

Here $n = P_{nh}/P_{hy}$, which compares the typical magnitude of non-hydrostatic to hydrostatic pressure, is given by

$$n = \frac{\gamma^2}{R_i} \quad (5)$$

Note that in Eq. (1) we have separated the pressure into hydrostatic, non-hydrostatic and surface pressure parts and, furthermore, we have introduced a tracer parameter q multiplying p_{nh}: In HPE, $q = 0$; in INS, $q = 1$.

We can now more clearly identify the non-hydrostatic and hydrostatic regimes in this rotating stratified fluid.

(i) The Non-hydrostatic regime [$n \geq R_o$]: horizontal gradients of p_{nh} are important in the evolution of the flow and cannot be neglected in Eq. (1).

(ii) The Transitional regime [$n \leq R_o$]: where non-hydrostatic effects no longer dominate and the flow is under increasing hydrostatic control.

(iii) The Hydrostatic regime [$n \ll R_o$]: as assumed in HPE.

In the rotating, stratified problem γ^2 must be compared with $R_i R_o$, rather than unity:

$$\gamma^2 \ll R_i R_o$$

for hydrostatic balance. Note that the familiar condition for hydrostatic balance, $\gamma = h/L \ll 1$, is a very special case pertaining only when $R_i R_o \sim 1$. For example, a fluid in which $\gamma \sim 1$ can still be hydrostatic if it is either rotating sufficiently rapidly or it is sufficiently stratified. The above can be expressed differently by expanding out and collecting terms thus:

$$\frac{n}{R_o} = \frac{f^2}{N^2}\frac{U}{fL} \ll 1 \quad \text{for hydrostatic balance} \quad (6)$$

a form which clearly demonstrates that strong stratification and high rotation both inhibit non-hydrostatic effects. In the ocean N/f ranges between zero and perhaps 100; the Rossby number from 10 to below 10^{-2}. In Table 1, we present n/R_o as a function of N/f and R_o; it should be compared with unity. It is clear that non-hydrostatic effects come in to play in very weakly stratified regions of the ocean (such as deep convection sites where, after convection, N/f is of order unity) and will be largest on small scales in swift currents where the Rossby

Table 1
Table showing the magnitude of the non-hydrostatic parameter $n/R_o = (f^2/N^2)(U/fL)$ as a function of f/N and U/fL

n/R_o		f/N		
		0.01	0.1	1
U/fL	0.01	10^{-6}	10^{-4}	0.01
	0.1	10^{-5}	10^{-3}	0.1
	1	10^{-4}	0.01	1
	10	10^{-3}	0.1	10

number is large. While it is clear that on the large scale, the hydrostatic approximation is an exceedingly good one (top left of table) as one moves towards the bottom right motions become increasingly non-hydrostatic (n/R_o large).

With the increasing power of computers, ocean models based on the HPEs are increasingly employed at horizontal resolutions comparable with the depth of the ocean—indeed the need to adequately resolve the geostrophic eddy scale (~ 10 km) demands such high resolutions. In those places where the water column is weakly stratified, such as deep water formation sites or mixed-layer regions, the hydrostatic approximation may not be adequately satisfied and the appropriateness of the HPEs must then be brought into question.

Is it possible, then, to build a model that (i) does not, a priori, assume hydrostatic balance so making it suitable for the study of unbalanced convective scales of motion and yet (ii) can be employed economically at large, hydrostatically balanced scales? Suppose at the outset we were to separate the pressure into hydrostatic and non-hydrostatic components. In the hydrostatic limit, one would just compute the pressure at one particular level in the ocean (it is convenient to choose the surface pressure) and then deduce the pressure hydrostatically at all other levels; in the non-hydrostatic limit, one must further determine p_{nh}. In the hydrostatic limit of INS, $q = 0$ but p_{nh} is *not* zero. However, *only its vertical variation is required* in Eq. (2) to drive the evolving vertical velocity. [2] Moreover, if $q \equiv 0$, the vertical velocity found from Eq. (2) yields *exactly* that which would have been deduced from the continuity equation had HPE been used.

More precisely, the non-hydrostatic pressure satisfies the following elliptic equation; taking ∇_h of Eq. (1) and $\partial/\partial z$ of Eq. (2) using Eq. (4), we obtain:

$$\frac{\partial^2 p'_{nh}}{\partial z^2} + \frac{qn}{R_o^2}\nabla_h'^2 p'_{nh} = \frac{1}{R_o}[\text{Source}]_{nh} \qquad (7)$$

which must be solved subject to appropriate (Neumann) boundary conditions. These are discussed at length in Marshall et al. (1997a). Thus if $q = 0$, the three-dimensional operator $\rightarrow (\partial^2)/(\partial z^2)$ and so can be solved trivially. Furthermore, if $n/R_o \leq 1$ then (even for full INS in which $q = 1$) the left hand side of Eq. (7) will be dominated by the vertical axis and an iterative solution of Eq. (7) will converge rapidly (see for example Hill and Marshall, 1995).

This, then, suggests our strategy; we separate the pressure into its hydrostatic and non-hydrostatic components. In the hydrostatic limit of INS, the non-hydrostatic pressure required to step w forward prognostically can be found directly (and rapidly) by solving a second order ODE. As non-hydrostatic effects become more important, the elliptic operator becomes more and more isotropic, and the three-dimensional inversion requires correspondingly more computational effort. However, the INS model, unlike HPE, asymptotes to the continuum as its resolution is increased.

2.2. Numerical strategy

2.2.1. Overview

The approach outlined above has been used by us to guide the construction of a model rooted in INS building on ideas developed in the computational fluids community. The numerical challenge is to ensure that the evolving velocity field remains non-divergent. Most procedures, including the one employed here, are variants on a theme set out by Harlow and Welch (1965), in which a pressure correction to the velocity field is used to guarantee non-divergence. The correction step is equivalent to, and is solved as, a three-dimensional Poisson problem for the pressure field with Neumann boundary conditions (7). A 'brute force', unthinking approach to the Poisson inversion requires prohibitive amounts

[2] Indeed even in HPE a p_{nh} is implied, and can be deduced from $w(t)$.

of computer time, and would render the INS model, even in its hydrostatic limit, uncompetitive with HPE. Moreover, the inversion demands 'global' connectivity between all points in the computational domain, presenting a challenge in mapping the model to a parallel computer because such connectivity requires communication right across the grid to the boundary. A major objective, therefore, was to design a Poisson solver that was efficient and could map well to parallel architectures, thereby making INS a powerful tool applicable to all scales of interest in oceanography.

2.2.2. Some details

We write the Boussinesq incompressible Navier Stokes equations describing our ocean model in semi-discrete form to second order in the time Δt, in which only time is discretized:

$$\frac{\underline{v}_{\mathrm{h}}^{n+1}-\underline{v}_{\mathrm{h}}^{n}}{\Delta t}=\underline{G}\boldsymbol{v}_{\mathrm{h}}^{n+\frac{1}{2}}-\nabla_{\mathrm{h}}\{p_{\mathrm{s}}+p_{\mathrm{hy}}+qp_{\mathrm{nh}}\}^{n+\frac{1}{2}} \tag{8}$$

$$\frac{w^{n+1}-w^{n}}{\Delta t}=\hat{G}_{w}^{n+\frac{1}{2}}-\frac{\partial p_{\mathrm{nh}}^{n+\frac{1}{2}}}{\partial z} \tag{9}$$

$$\frac{\partial w^{n+1}}{\partial z}+\nabla_{\mathrm{h}}\cdot\underline{v}_{\mathrm{h}}^{n+1}=0 \tag{10}$$

Eqs. (8)–(10) describe the time evolution of the flow from step n to $n+1$; $\boldsymbol{v}=(\boldsymbol{v}_h,w)$ is the velocity in the horizontal and the vertical, and the G terms comprise inertial, Coriolis, metric, gravitational, and forcing/dissipation terms. They are written out in full in Marshall et al. (1997b) where time-stepping details may also be found. The $\hat{}$ denotes that balancing terms, involving hydrostatic pressure and gravity, have been canceled out to better condition (9) for numerical integration.

Eqs. (8)–(10), in dimensional form, are solved in the irregular geometry of an ocean basin in a spherical polar coordinate system (see Fig. 2a) using finite-volume techniques. The velocity normal to all solid boundaries is zero, and a rigid lid or an (implicit) free surface is assumed at the upper boundary. (For brevity we have not written down equations for temperature and salinity but these too must be stepped forward to find, by making use of an equation of state, the density ρ).

In Eq. (8), the pressure has been separated into surface, hydrostatic and non-hydrostatic components thus:

$$p(\lambda,\sigma,z)=p_{\mathrm{s}}(\lambda,\sigma)+p_{\mathrm{hy}}(\lambda,\sigma,z)+qp_{\mathrm{nh}}(\lambda,\sigma,z) \tag{11}$$

where (λ,ϕ,z) are the latitude, longitude and depth, respectively. The first term, p_{s}, is the surface pressure; it is solely a function of horizontal position and time. The second term, p_{hy}, is the hydrostatic pressure defined in terms of the weight of water in a vertical column above the depth z:

$$\frac{\partial p_{\mathrm{hy}}}{\partial z}+g'=0 \tag{12}$$

where g' is the 'reduced gravity' $g(\delta\rho)/(\rho_{\mathrm{ref}})$, and $\delta\rho$ is the departure of the density from a reference profile; ρ_{ref} is the constant reference density. The third term is the non-hydrostatic pressure, p_{nh}. In INS, w is found using Eq. (9), from which large and balancing terms involving the hydrostatic pressure and gravity (12) have been canceled (remaining terms are represented by $\hat{G}_{\mathrm{w}}$) to ensure that it is well conditioned for prognostic integration. In HPE, Eq. (9) is not used; rather w is diagnosed from the continuity relation (10). In the hydrostatic limit ($q=0$) only p_{hy} and p_{s} are required in Eq. (1). Eq. (12) is used to find p_{hy}; the surface pressure, p_{s}, is found by solving the following two-dimensional elliptic problem that ensures non-divergent depth-integrated flow:

$$\nabla_{\mathrm{h}}\cdot H\nabla_{\mathrm{h}}\,p_{\mathrm{s}}^{n+\frac{1}{2}}=\nabla_{\mathrm{h}}\cdot\overline{\underline{G}_{\boldsymbol{v}_{\mathrm{h}}}^{n+\frac{1}{2}}}^{H}-\nabla_{\mathrm{h}}\cdot\overline{\nabla_{\mathrm{h}}p_{\mathrm{hy}}}H \tag{13}$$

(Here $\overline{}^{H}$ represents the vertical integral over the local depth, H, of the ocean and the subscript h denotes horizontal).

In INS, q is set equal to unity and p_{nh} must be determined. It is found by inverting a three-dimensional elliptic equation ensuring that the local divergence vanishes:

$$\nabla^{2}p_{\mathrm{nh}}^{n+\frac{1}{2}}=\nabla\cdot\underline{G}^{n+\frac{1}{2}}-\nabla_{\mathrm{h}}^{2}(p_{\mathrm{s}}+p_{\mathrm{hy}}) \tag{14}$$

where ∇^2 is a full three-dimensional Laplacian operator.

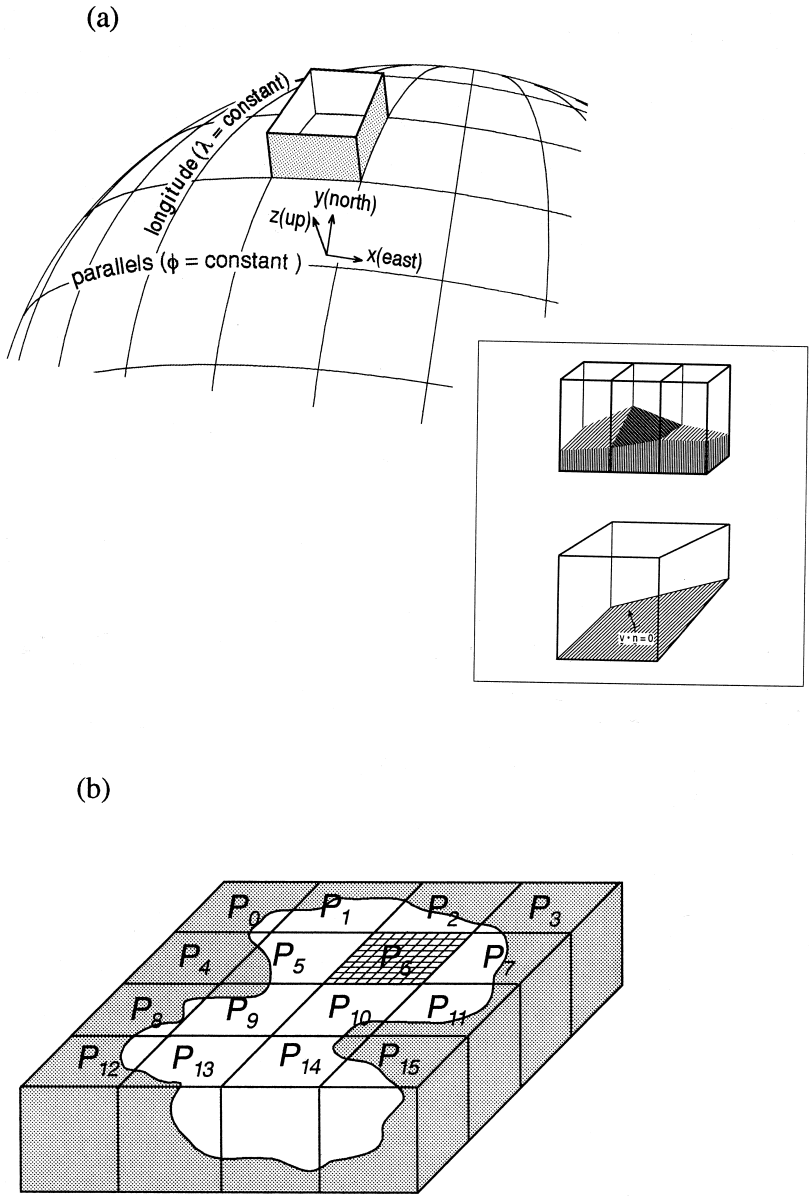

Fig. 2. (a) The computational domain is carved in to a large number of finite volumes (which we call zones). Each zone is characterized by a volume and six surface areas. Velocities and fluxes are defined and held normal to the faces of the zones assuring that the divergence operator has a simple and compact form. The faces of the zones are chosen to be coincident with the three orthogonal coordinate axes, sketched here for a latitude/longitude/vertical grid. Inset: zones adjacent to a solid boundary may be shaved allowing the grid to be 'sculpted' to fit an irregular boundary (see Adcroft et al., 1997). The velocity normal to any solid boundary vanishes. (b) Domain decomposition adopted in the mapping of the model on to a parallel computer using the 'data-parallel' approach. In the schematic diagram the ocean is decomposed in to columns distributed over 16 processors P of a parallel computer. The thick black lines indicate regions of the domain assigned to the same processor. The thin lines indicate the 'volumes' within each subdomain.

We see that in addition to the two-dimensional inversion required in HPE (as in, for example, Bryan, 1969 or Ducowicz et al., 1993) INS requires the solution of a three-dimensional elliptic problem; this is the overhead of INS relative to HPE. However, the three-dimensional problem is preconditioned by multiplying through by an operator (called the preconditioner) which, in the hydrostatic limit, is an exact inverse of $\partial^2/\partial z^2$ and so leads to a single algorithm that seamlessly moves from non-hydrostatic to hydrostatic limits; the preconditioner is an exact inverse in the hydrostatic limit and yields a solution directly in that limit. Thus, when employed to study the large-scale, the model is 'fast', competitive with the fastest ocean climate models in use today based on the hydrostatic primitive equations. Yet, as the resolution is increased, the model dynamics asymptote smoothly to the continuous Navier Stokes equations and so can be used to address small-scale processes. Furthermore, as noted by Browning et al. (1990), adoption of INS in the hydrostatic limit yields a better posed system of equations.

2.3. Numerical discretization and implementation

Solution of the Poisson equation is an important consideration in the choice of model discretization and the manner in which the algorithm is mapped on to a parallel computer. A robust and compact discrete form of ∇^2 results if the divergence operator is represented using finite volumes in which the physical domain is carved up in to many small volumes and the velocity components (and property fluxes) are defined normal to the faces that define the volumes. The use of finite volume methods also makes possible a novel treatment of the boundary in which volumes abutting the bottom or coast may take on irregular shapes and so be 'sculpted' to fit the boundary (see Fig. 2a, Marshall et al., 1997b, and in particular Adcroft et al., 1997).

The algorithm was developed and implemented on a 128-node CM5, a massively parallel distributed-memory machine in the Laboratory for Computer Science (LCS) at MIT. The code was written in CMFortran, a data-parallel FORTRAN, closely related to High Performance Fortran (HPF). The algorithm was also coded in the implicitly parallel language Id, permitting a multithreaded implementation on MIT's data flow machine MONSOON. The programming issues are developed more fully in Shaw et al. (1998), where implicitly parallel multithreaded and data parallel implementations are compared.

In deciding how to distribute the model domain over the available processors on a distributed memory machine, we had to bear in mind that the most costly task in the algorithm is finding the pressure field. A preconditioned conjugate gradient method is used to solve Eqs. (13) and (14). The preconditioning operator entails nearest-neighbor communication between adjacent cells in the horizontal and communication over all cells in the vertical. Accordingly, in the parallel approach, we decompose the computational domain into vertical columns. In this way, the workload is distributed across processors laterally in equally sized rectangles (Fig. 2b).

Having outlined our numerical strategy, in the next section we go on to illustrate its use in the study of deep convection plumes and baroclinically unstable chimneys.

3. Non-hydrostatic modeling of convection and baroclinic instability

3.1. Convection

The numerical model described in Section 2 has been used extensively to study oceanic convection and test out scaling ideas that pertain to rotating convection. Here we present results from one such experiment (Fig. 3) in which convection, driven by vigorous cooling from the surface (-800 W/m^2) is modeled at very high (50 m) horizontal resolution; the dynamics may be expected to be strongly non-hydrostatic.

The domain is a doubly periodic box of side ~ 10 km and depth 2 km of initially resting unstratified, rotating fluid. Isotropic Laplacian diffusion of heat and momentum was employed with a Prandtl number of unity and the flux Rayleigh number $\mathrm{Ra_f} = 10^9$. A linear equation of state was used (but see Sander et al. (1995) where a more realistic equation of state is considered). The numerical experiment used 192 $\times$ 192 grid-cells in the horizontal with 40 non-equidistant levels in the vertical: 6 m near-surface resolution declining to 100 m at mid-depths. Inte-

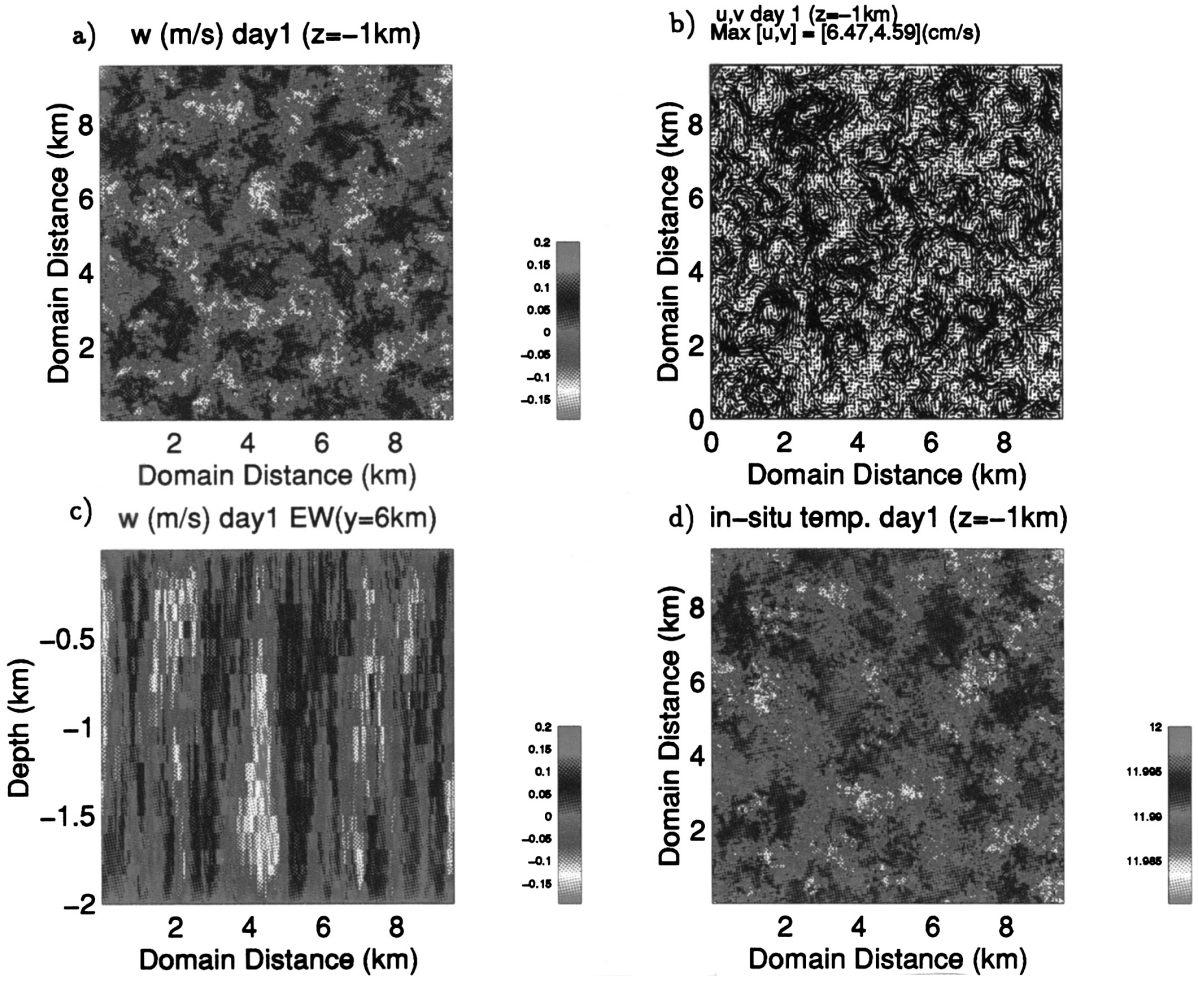

Fig. 3. Numerical simulation of convection induced by surface cooling in an initially neutral, unstratified rotating fluid in $10 \times 10 \times 2$ km doubly periodic box. Fields are plotted after one day of integration. The horizontal resolution of the model is 50 m. The vertical resolution varies from 6 m at the surface to 100 m at mid-depths. (a) horizontal of vertical velocity, at mid-depths $z = -1$ km. (b) pattern of horizontal currents at $z = -1$ km. (c) an east–west, chosen to pass through the downwelling center apparent at $x \sim 4.5$ km. (d) a horizontal of in situ temperature, at mid-depths $z = -1$ km.

grated forward with a timestep of 10 s each day of integration took 3 h of CPU time on a 64 node CM5 computer.

The separation of the pressure into its constituent parts is very effective at reducing computation, even in this simulation where non-hydrostatic effects *are* important (n, evaluated from the evolving fields in Fig. 3, ranges from 0.1 to 1). The number of three-dimensional iterations required to solve Eq. (14) is reduced by almost an order of magnitude when the surface pressure is 'taken out' of the three-dimensional problem by solving for it separately first. Moreover, in a hydrostatic calculation, the surface pressure must be found anyway, and so the cost of the pressure inversion of INS relative to HPE is only a factor of 4 in this particular simulation. Instead, had we inverted for p directly, INS would have been more than 35 times slower than HPE. It should be emphasized that here we have not exploited the simple geometry of the model configuration (a flat-bottomed doubly-periodic domain) because our aim is to develop methods that can be employed in

domains as complex as ocean basins; the method outlined here is equally applicable in irregular domains (see the simulation of the entire Mediterranean ocean described in Section 4, for example).

In the face of persistent cooling, [3] plumes penetrate progressively deeper in to the interior, lowering the mean base of the convective layer. In time, they distribute the influence of the intense surface heat loss over the whole depth of the ocean. Fig. 3 shows currents and temperatures after 24 h of sustained surface forcing. Fig. 3a shows a horizontal of vertical velocity at mid-depths indicating that the plumes have scales of ~ 1 km. As expected, the vertical velocity field is closely correlated with the in situ temperature (Fig. 3d: cold water sinking (with velocities approaching 15 cm s^{-1} in plume-centers; warm water rising to compensate in between).

3.1.1. Scaling ideas

Oceanic convection is of interest, in part because it represents a mode of convection which is in a different parameter regime from atmospheric convection. The natural Rossby number:

$$R_0* = \frac{l_{\rm rot}}{H} = \frac{u_{\rm rot}}{fH} = \left(\frac{B}{f^3H^2}\right)^{\frac{1}{2}} \quad (15)$$

$$l_{\rm rot} = \left(\frac{B}{f^3}\right)^{\frac{1}{2}};\ u_{\rm rot} = \left(\frac{B}{f}\right)^{\frac{1}{2}} \quad (16)$$

(Maxworthy and Narimousa, 1994; Jones and Marshall, 1993), based on external parameters B (m^2 s^{-3}) the buoyancy forcing, f (s^{-1}) the Coriolis parameter and H the depth m of the ocean. R_o* compares the scale $l_{\rm rot}$ at which convection comes under the influence of the Earth's rotation, to the total depth of the convection H. This non-dimensional number has played a central role in the development of ideas about plume-scale and chimney-scale dynamics in the ocean (see Marshall et al., 1994; Marshall and Schott, in press). It turns out that R_o* is *large* in the atmosphere but *small* in the ocean. If the fluid is stiffened by rotation on the convective scale (R_o* small) then downwelling induced by surface forcing B, in the presence of rotation f, generates strong swirling motion of speed $u_{\rm rot}$ due to the squashing of Taylor Columns.

In order to test scaling ideas, a range of similar numerical experiments was carried out in which R_o* was ranged through three orders of magnitude by varying the Coriolis parameter; in the reference simulation, shown in Fig. 3, $f = 10^{-4}$ s^{-1}. The range of R_o*, 0.01 to 10, is typical of values in open-ocean convection regions.

In Fig. 4a, we plot the horizontal velocity variance at day 2 as a function of depth for this series of experiments, normalized with respect to the non-rotating scaling $u_{\rm norot} = (BH)^{1/3}$ (Deardorff and Willis, 1967). Velocities in an (essentially) non-rotating experiment, where $f = 10^{-6}$ s^{-1}, indeed scale as $u_{\rm norot}$—the curve is centered on unity in Fig. 4a. However, we see that at higher rotation, typical eddy velocities decrease as the rotation rate increases, as suggested by the scaling (16). Fig. 4b again plots the horizontal velocity variance against depth but now normalized with respect to $u_{\rm rot}$, Eq. (16). The normalized velocities from all the high rotation experiments collapse on to the same line centered around unity; $u_{\rm rot}$ is indeed the velocity scale adopted by the plumes at high rotation. Note that it is only velocities from the $f = 10^{-6}$ s^{-1} experiment that appear anomalous when scaled with respect to the rotational velocity scaling $u_{\rm rot}$.

Laboratory experiments reported by, for example, Maxworthy and Narimousa (1994) and Coates et al. (1995), suggest that the numerical experiments presented above, and in Jones and Marshall (1993), over-emphasize the role played by rotation in oceanic plume-scale dynamics. The consensus of the laboratory experimentalists is that rotational effects are only felt when $R_o* < 0.1$, rather than for $R_o* < 0.7$ or so as in our numerical experiments. This issue can only be resolved through the careful design of further numerical experiments, but the way forward is not clear.

The approach of Jones and Marshall (1993) leading to the numerical solutions shown in Fig. 3 is that of a Large Eddy Simulation (LES) and uses very crude closure assumptions (Laplacian diffusion of heat and momentum with constant diffusivities) and on those grounds has been criticized by Sander et al. (1995) and Coates et al. (1995). More sophisticated

[3] A random modulation of the forcing on the grid-scale about the specified mean value was used to trigger convection.

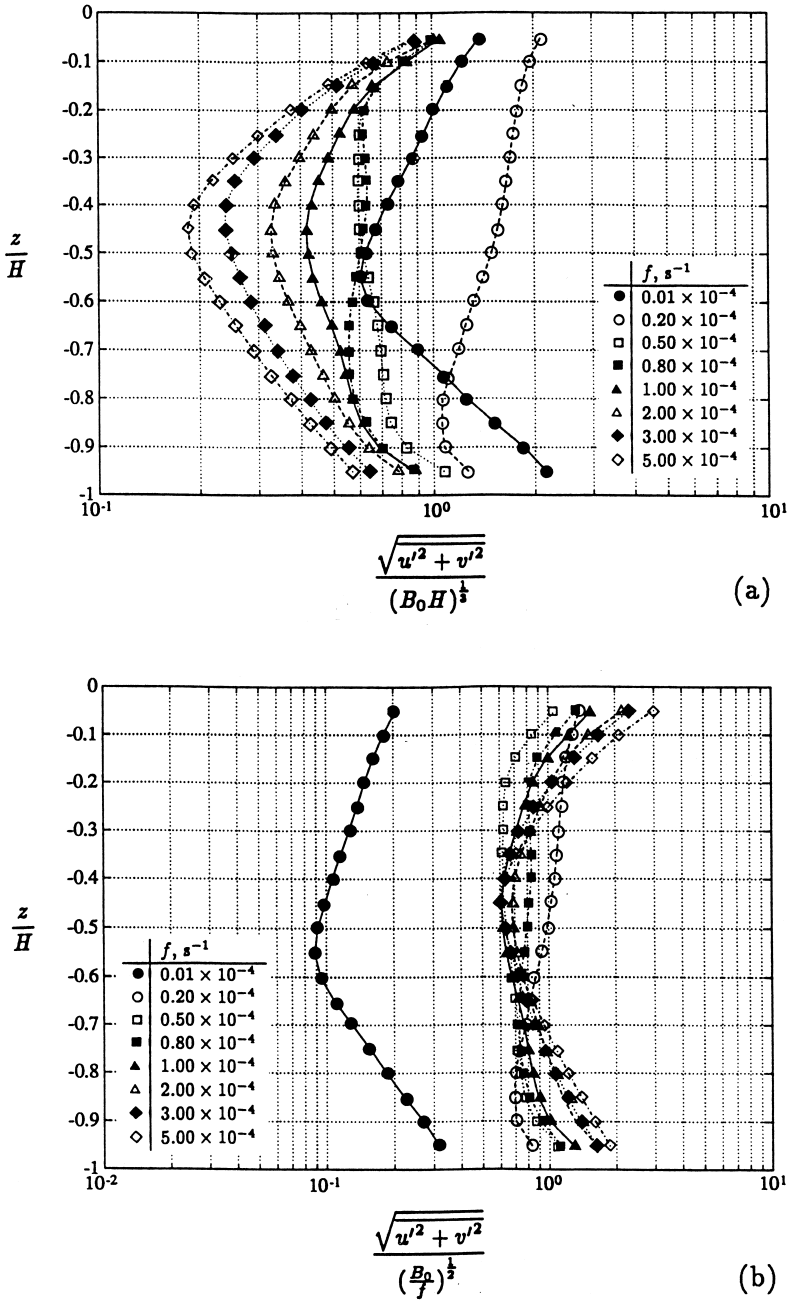

Fig. 4. Horizontal velocity variance plotted as a function of depth from a series of numerical experiments, including the one presented in Fig. 3, in which R_o* was varied through 3 orders of magnitude. (a): normalized with respect to the non-rotating scaling $(B_0H)^{1/3}$ (b) normalized with respect to the rotating scaling u_{rot}.

closure schemes exist (more often than not tuned to atmospheric observations), but even the most sophisticated LESs assume the turbulence is isotropic and homogeneous and thus make gross assumptions about the nature of the small scale turbulence (a critical review of the method in the atmospheric context is

given by Mason, 1994; see Garwood et al., 1994 and Denbo and Skyllingstad, 1994, for examples of LES applied to ocean convection). However rotating convection is strongly anisotropic—both because of the nature of the plumes, which are stiffened by rotation, and because of the overall organization of the flow by rotation. The advantage of LES is that simulations with Reynolds numbers, Re, approaching realistic values can be made; its disadvantage is that results obtained using that method may depend on assumptions implicit in the assumed closure hypotheses.

An alternative approach, that of direct numerical simulation (DNS), is one in which all the dynamically active scales of motion, down to the Kolmogorov scale, are resolved; it is being pursued by Julien et al. (1996) and Kerr et al. (1995) but, because of the enormous computational cost, is limited in the range of Re it can study. However, anisotropies in mixing properties, and boundary layer processes, can be examined without any pre-imposed bias in DNS. Since realistic Re cannot be examined, the DNS approach instead searches for scaling behavior in the solutions, and then extrapolates to realistic values, assuming that the flow remains in the same dynamical regime.

The underlying hydrodynamics explored in the above numerical experiments can be modified, but not fundamentally changed, by thermobaric effects. Sander et al. (1995) repeat the Jones and Marshall (1993) experiments with a more realistic equation of state and show that thermobaric effects lead to enhanced vertical accelerations in the water column. Garwood et al. (1994), using an LES model also find important modifications to the vertical profile of buoyancy flux in deep polar sea thermal convection. They also show that thermobaric effects make it possible to generate conditional instabilities if salinity stratification is partially balanced by thermal stratification (as for example in the Greenland Sea). These classes of instability are mathematically analogous to conditional instabilities of a moisture-laden atmosphere (reviewed by Emanuel, 1994).

3.2. The switch-over from convection to baroclinic instability

What happens if we impose a buoyancy forcing which varies in space thus inducing a mixed layer which is deeper and hence colder in one place than another, as in the schematic diagram shown in Fig. 1b?

In Fig. 5 a resting, stratified fluid ($N/f = 10$) modeled using INS was subject to a steady buoyancy loss through the sea surface. The cooling is independent of down-channel coordinate but increases across the channel following a hyperbolic tangent variation. Thus, in the southern third of the channel there is weak surface forcing, in the northern third fairly constant densification equivalent to a heat loss of 800 W m^{-2}, and a sharp transition in between. As in the experiment described in Section 3.1, convection was triggered by the inclusion of grid-scale noise in the forcing field. A linear equation of state is specified dependent on temperature alone and the resolution is sufficient to represent gross aspects of the convective process.

The channel was modeled using a singly periodic $200 \times 120 \times 20$ grid (horizontal resolution of 250 m, mean vertical resolution 100 m). Integrated forward with a timestep of 120 s, the channel experiment required one hour of CPU time on a 32 node CM5 computer for each month of simulation. Because of the presence of relatively strong stratification in this experiment, non-hydrostatic effects are somewhat less important here than in the unstratified case ($n = 0.1$), and an even greater improvement in performance is seen when the pressure separation is made. In using our INS model, the number of three-dimensional iterations required to solve Eq. (14) is reduced by an order of magnitude by solving for the surface pressure separately first. In this case, the relative cost of the pressure inversion of INS vs. HPE is only a factor of 3; had we inverted for p directly, INS would have been more than 30 times slower than HPE.

For the first few days of integration a mixed layer of depth, h, develops according to a simple, non-rotating, one-dimensional law which predicts the depth of mixing due to the upright overturning. Namely:

$$h = \frac{\sqrt{2\,Bt}}{N} \tag{17}$$

where B is the buoyancy flux through the surface at time t and N the Brunt–Väisällä frequency. Initially,

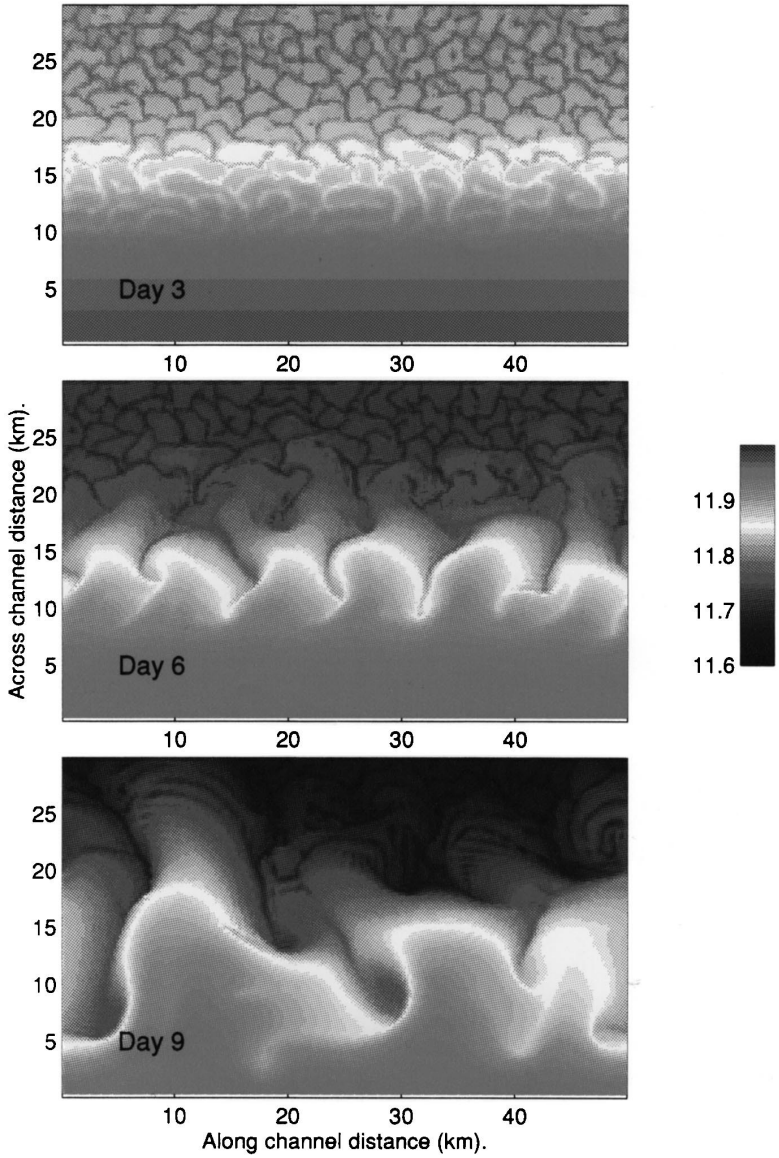

Fig. 5. INS simulation of an initially stratified fluid resting in a 2 km-deep channel and subject to cooling from its upper surface. Temperature at a depth of 65 m is plotted. The cooling varies across the channel in the manner of a hyperbolic tangent. Plume-scale (non-hydrostatic) convection at day 3 gives way to finite amplitude baroclinic instability at day 6. By day 9 a mature field of geostrophic turbulence exists.

the vertical mixing is facilitated by upright convection as in the previous example. But, as a result of the developing density gradient across the channel, the flow adjusts to thermal wind balance and the flow evolves from plume-scale convection at day 3 to finite amplitude baroclinic instability at day 6, with a mature field of geostrophic turbulence by day 9. A surface intensified jet emerges in balance with the across channel temperature gradient, with the eddying component of the flow dominating. Since there is no stress applied at the ocean surface the global zonal momentum cannot change and eastward

flow at the surface is compensated by a westward current below. The length-scale for the baroclinic instability at day 6 is around 5 km, in reasonable agreement with predictions from linear instability analysis (see Haine and Marshall, 1998).

A study of the potential vorticity (PV) field (not shown) reveals the key dynamical processes at work. The largest scale features are the baroclinic eddies which mix southern, high ambient PV fluid with the convectively modified low PV water to the north. There is a strong gradient between these two water types with a relatively small amount of water with intermediate PV; in the north patches of negative PV identify the energetic plumes which draw the PV and buoyancy from the fluid. But there is also a systematic lateral flux achieved by the eddies which be-

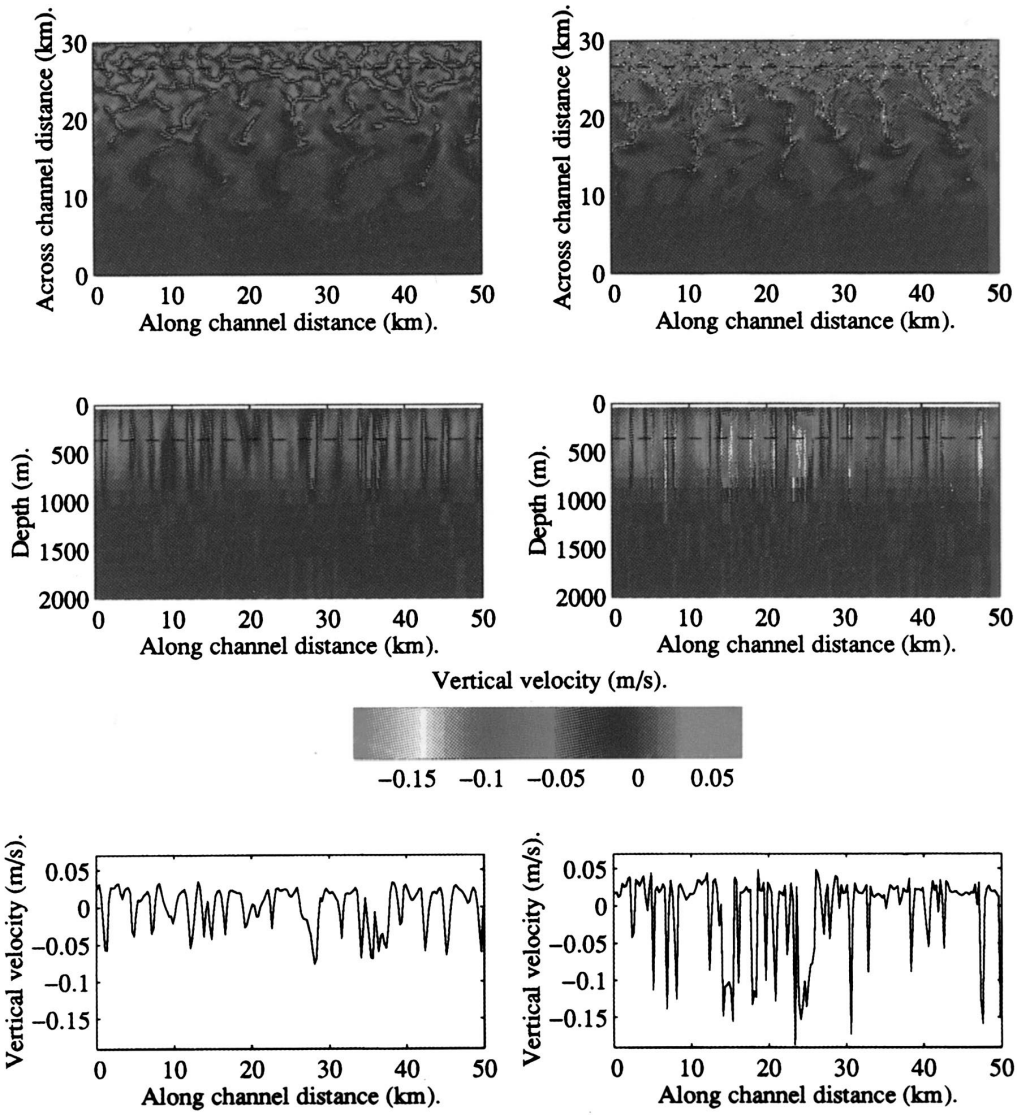

Fig. 6. The vertical velocity obtained by (on the left) integration of INS at day 6 of the mixed-layer channel calculation shown in Fig. 5 and (on the right) obtained using HPE, all other model details being exactly the same. The bottom two panels compare $w(x, y = 27$ km, $z = 400)$ from the non- hydrostatic (left) and hydrostatic (right) runs, again at day 6.

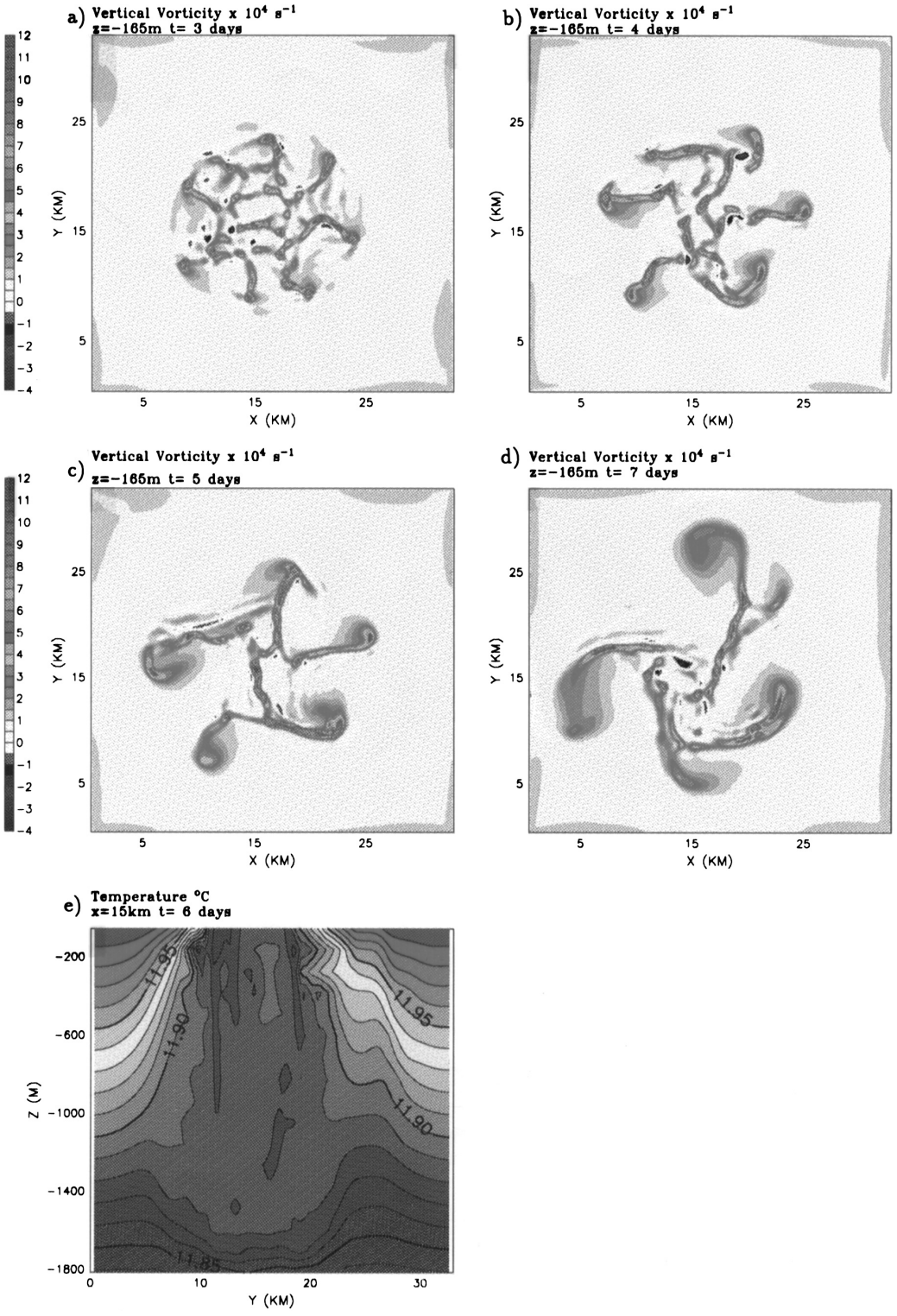
a) Vertical Vorticity x 10⁴ s⁻¹
z=−165m t= 3 days
b) Vertical Vorticity x 10⁴ s⁻¹
z=−165m t= 4 days
c) Vertical Vorticity x 10⁴ s⁻¹
z=−165m t= 5 days
d) Vertical Vorticity x 10⁴ s⁻¹
z=−165m t= 7 days
12 11 10 9 8 7 6 5 4 3 2 1 0 −1 −2 −3 −4
Y (KM)
X (KM)
5 15 25
e) Temperature °C
x=15km t= 6 days
−200 −600 −1000 −1400 −1800
Z (M)
0 10 20 30
Y (KM)
11.95
11.90
11.85

come the major contribution to the buoyancy budget in the south where the cooling is weak.

Thus, in the presence of lateral buoyancy gradients, we observe a change in the manner in which buoyancy is drawn through the mixed layer. In nature such gradients are always present, either in the ambient stratification or the prevailing forcing; thus, one expects that if those inhomogeneities persist, mixed-layer baroclinic instability will ultimately take over from upright convection as the dominant mode of buoyancy transfer.

3.3. Hydrostatic modeling of convection

Fig. 6 repeats the mixed-layer calculation presented in Section 3.2 but with HPE rather than INS. It is interesting to observe that HPE attempts to represent the convective overturning of the fluid column even though acceleration terms in the vertical momentum equation are absent. Statically unstable columns are overturned, through appropriate homogenization of the temperature and salinity fields, by HPE but at the grid-scale of the model and the resulting field of vertical velocity is up to twice as strong as in INS and much less smooth and coherent. This is just as one would expect from linear Rayleigh theory; the static instability of a column is more vigorous and occurs at smaller spatial scales in hydrostatic compared to non-hydrostatic convection. Our split solver approach renders INS (left column) only 3 times slower that HPE (right column).

3.4. Simulation of an open-ocean chimney

Now let us consider a stratified ocean exposed to surface buoyancy loss localized at the center of a box rather than varying across a channel. Surface waters beneath the cooling disc will become dense and overturn forming a convectively modified layer of depth h. Toward the center of the cooling disc, fluid will not be aware of the spatial inhomogeneity in the cooling—here the mixed layer will deepen, at least initially, in a one-dimensional manner through the agency of plumes in accordance with Eq. (17). But ultimately, and as is vividly demonstrated in Fig. 8, convection gives way to baroclinic instability.

Just as in the channel scenario this integration includes non-hydrostatic dynamics as plumes penetrate into the fluid interior, but again n is relatively small, $n \sim 0.1$. Integrated forward with a one minute timestep this integration requires one hour of 32 node CM5 compute time for each day of integration. Using the split solver the INS overhead relative to HPE is a factor of 3. Without the separated pressure solver, INS simulation would require 30 times more computer time than the HPE counterpart.

Since away from the disc of cooling the stratification takes up its ambient value while in the center of the chimney, the stratification is being eroded away, then around the periphery of the chimney isopycnal surfaces will bow up from their resting level to cut the ocean's surface. Associated with the tilting isopycnal surfaces, a thermal wind is set up establishing a 'rim current' around the chimney within a day or so. The width of the rim current region and its baroclinic zone will be initially of the order of the Rossby radius of deformation. Moreover, the rim current in thermal wind balance will be susceptible to baroclinic instability.

So at the center of the chimney the mixed-layer deepens according to Eq. (17) until the growing baroclinic instability begins to sweep the water surrounding the cooling disc in to the chimney and carry convected fluid outward and away below. If the cooling persists, the rate of deepening will be slowed, and may eventually be halted by finite-amplitude baroclinic eddies. This limit, in which the lateral flux balances loss from the surface, was studied in the context of a 'heton' model in Legg and Marshall (1993) and Legg et al. (1996) as well as through more conventional numerical models and laboratory experiments in Visbeck et al. (1996) and Whitehead et al. (1996).

Fig. 7. Numerical simulation of an open-ocean convective chimney using INS. In (a), (b), (c) and (d) the vertical component of absolute vorticity is plotted at a depth of $\sim$ 200 m after 3, 4, 5 and 7 days respectively. Below, in (e), we show a vertical of temperature through the middle of the chimney at day 6. Again we see that plume-scale convection (evident at day 3) gives way to finite amplitude baroclinic instability (from day 4 onwards).

The sequence of events is clearly demonstrated by integration of INS. Fig. 7 presents maps of the vertical component of absolute vorticity near the surface from a simulation of the deepening of a chimney in to a stratified resting fluid in which, N, measured against the Coriolis parameter, f, is $N/f = 5$. Buoyancy was extracted from a resting, stratified fluid, over a disc 16 km in diameter at the center of the domain. The resolution of the model is sufficient to resolve baroclinic eddies, but also gross aspects of the convective plumes themselves. By day 3 convective plumes are present in the interior of the cooling region 'burrowing' in to the stratified fluid beneath; a rim-current is beginning to develop meanders, evidence of baroclinic instability. By the end of day 4, a wave-number five baroclinic instability is clearly visible while upright convection has diminished in intensity. Finally, at day 6, the plumes have all but disappeared and five large instability eddies are breaking the chimney apart, sweeping light fluid inwards and thereby arresting the downward penetration of the mixed-layer.

4. Incompressible Navier Stokes in the hydrostatic limit; simulation of the Mediterranean using INS

We have described the modeling of convection and baroclinic instability with INS. Can we employ the same algorithm with economy to study large-scale processes? The circulation of the Mediterranean with its highly irregular topography and small deformation radius provides a challenge.

Fig. 8 plots the current field at 40 m from a $1/4°$ resolution Mediterranean simulation in March of year 14 (using INS (i.e., in which $q = 1$ in Eq. (8))). The model has 184×63 grid-cells in the horizontal with 19 non-equidistantly spaced levels in the vertical: 10 m near-surface resolution declining to 500 m at depth. In this simulation n is only $\sim 10^{-4}$; the simulation is to all intents and purposes hydrostatic. However, because we employ the split pressure solver, the INS method can still be applied. In this limit the non-hydrostatic pressure inversion reduces to a one-dimensional ODE, as discussed in Section 2.1. The overhead of INS is negligible because the ODE along the vertical axis can be performed directly, and rapidly, in a single sweep using L-U decomposition. The simulation took 3 h of CPU time per year on 64 nodes of a CM5. If the pressure splitting were not exploited then p would have to be solved for from the full three-dimensional Laplacian and INS would have been 30 times slower than HPE.

The model was initialized with the annual mean Brasseur climatology (Brasseur et al. (1996)), and spun-up for 10 years. From then on it was forced with ECMWF (European Centre for Medium Range Weather Forecasting) twice-daily surface wind-stress

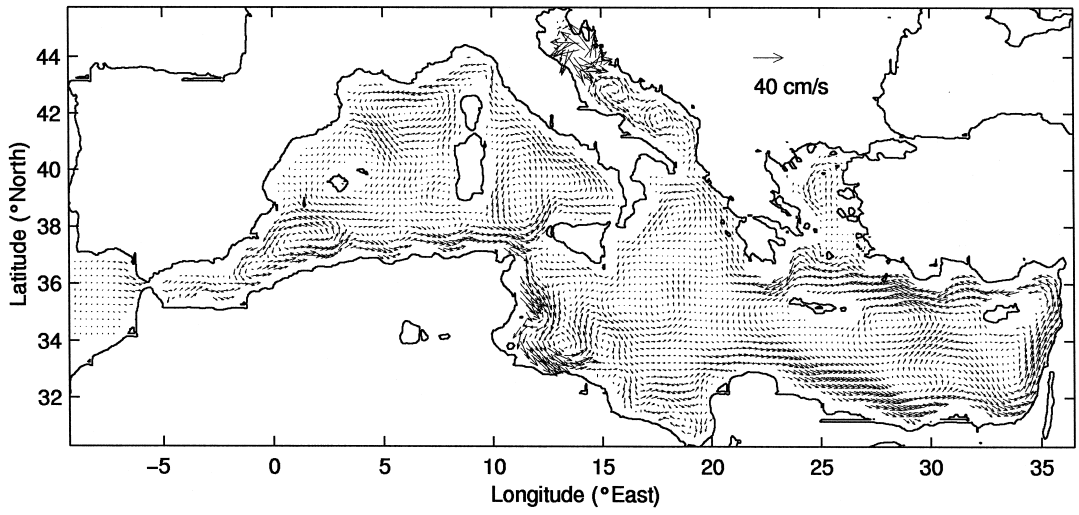

Fig. 8. The circulation produced in a $1/4°$ resolution INS Mediterranean simulation. Shown here are currents at a depth of 40 m.

and boundary conditions. The open boundary at Gibraltar was forced by tuning the salinity gradient in the eastern Atlantic to reproduce a realistic Algerian current.

Principal features, including the Liguro–Provencal current, the cyclonic circulation in the Gulf of Lions, and the Algerian current in the western basin are present, as are the Rhodes Gyre and Mersa Matruh circulations in the eastern basin. In general, the current systems are perhaps somewhat broader than is observed; the typical radius of deformation in rather small in the Mediterranean—only 15 km—suggesting that very much higher resolution is required to resolve the narrowness of the currents and their instabilities. The Alboron gyre is absent, for example, and the instabilities observed in the Algerian current are not present.

The calculation described here was combined by Menemenlis et al. (1997) with tomographic inversions of the thermal structure of the Western Mediterranean taken by Send et al. (1977), to estimate the state of the circulation.

5. Conclusions

We have outlined the rationale behind, and presented illustrative calculations from, an INS model which can relax the hydrostatic approximation and yet remain competitive with models that assume hydrostatic balance in that limit. The pressure field, which ensures that evolving currents remain non-divergent, is found by inversion of a three dimensional elliptic operator subject to Neumann boundary conditions. A major objective has been to make this inversion, and hence non-hydrostatic modeling, efficient. By separating the pressure in to surface, hydrostatic and non-hydrostatic components, and carefully preconditioning the resulting coupled 2-D and 3-D elliptic equations, a simple and efficient algorithm results. The approach maps naturally on to a parallel computer and suggests a domain decomposition that allocates entire vertical columns of the ocean to each processing unit. The resulting model is efficient and scalable and suitable for the study of the ocean circulation on horizontal scales less than the depth of the ocean, right up to global scale.

This methodology could be readily incorporated in to existing hydrostatic models allowing them to move smoothly from hydrostatic to non-hydrostatic limits; in the hydrostatic limit our INS algorithm (even though it is prognostic in w) is equivalent to, and no more demanding of computer resources than, a hydrostatic model. But, unlike a hydrostatic model, as the resolution of INS is increased it can be used to address small-scale phenomenon which are not hydrostatically balanced. Even in experiments of resolved convection using INS, where non-hydrostatic effects play a central role, separation of the pressure field in to its component parts leads to great savings. The resulting model is uniquely versatile with myriad possible applications. In the hydrostatic limit, it can be used in a conventional way to study the general circulation of the ocean in complex geometries. But because the algorithm is rooted in INS, it can also address (for example) (i) small-scale processes in the ocean such as convection in the mixed layer, (ii) the scale at which the hydrostatic approximation breaks down, and (iii) questions concerning the posedness of the hydrostatic approximation raised by, for example, Browning et al. (1990). It is interesting to note that—as described in Brugge et al. (1991)—the incompressible Navier Stokes equations developed here are the basis of the pressure-coordinate quasi-hydrostatic atmospheric convection models developed by Miller (1974).

Finally, we anticipate that hydrodynamical engines rooted in INS will be increasingly used as improved computational technology (see, e.g., Hill and Shaw, 1996) affords higher and higher resolutions.

Acknowledgements

This research was supported by grants from TEPCO, the Office of Naval Research and the EC Mermaids project. The model was developed on the CM5 housed in the Laboratory for Computer Science (LCS) at MIT as part of the SCOUT initiative. Much advice and encouragement on computer science aspects of the project was given by Arvind of LCS. Lev Perelman helped develop the strategy devised to solve our elliptic problems.

Appendix A. Incompressible Navier Stokes in the hydrostatic, geostrophic limit

We derive here the non-dimensional equations used in Section 2 to identify hydrostatic and non-hydrostatic regimes and to study the behavior of the incompressible Navier Stokes model in the hydrostatic, geostrophic limit.

We write down the momentum and thermodynamic equations for an incompressible Boussinesq fluid in Cartesian coordinates, non-dimensionalize them, and go on to consider the balance of terms when the flow is close to hydrostatic and geostrophic balance:

$$\frac{D\mathbf{v_h}}{Dt} + \nabla_h(p_s + p_{hy} + p_{nh}) + f\boldsymbol{k}\times\mathbf{v_h} = 0 \tag{18}$$

$$\frac{Dw}{Dt} + \frac{\partial p_{nh}}{\partial_z} = 0 \tag{19}$$

$$\frac{D_h b}{Dt} + N^2 w = 0 \tag{20}$$

$$\nabla\cdot\mathbf{v} = 0 \tag{21}$$

where:

$$\frac{D}{Dt} = \mathbf{v_h}\cdot\nabla + w\frac{\partial}{\partial z} \tag{22}$$

and $\boldsymbol{k}$ is a unit vector directed vertically upwards, and f is the Coriolis parameter.

To simplify our analysis, we have assumed an equation of state in which the density is a linear function of T and S (and independent of p); 'b' is the buoyancy:

$$b = -g\frac{\delta\rho}{\rho_{ref}}$$

where the density is, separating out a constant reference value and an ambient stratification, $\rho_0(z)$, typical of the fluid under study:

$$\rho = \rho_{ref} + \rho_0(z) + \delta\rho(x,y,z,t)$$

and:

$$N^2 = -\frac{g}{\rho_{ref}}\frac{\partial\rho_0}{\partial z}$$

is the stratification.

Note that in the above $p = \delta_p/\rho_{ref}$ has been separated in to its hydrostatic, non-hydrostatic and surface pressure components. Furthermore the hydrostatic pressure (which satisfies the relation $\partial p_{hy}/\partial z + b = 0$) has been canceled out with gravity in Eq. (19).

A.1. Dimensionless equations

We now scale the variables thus:

$\mathrm{v_h}$ by U; w by W

x by L; z by h

p_s, p_{hy} by P_{hy}; p_{nh} by P_{nh}

f by F

b by $g\frac{\rho_1}{\rho_{ref}}$; N^2 by $\frac{g}{h}\frac{\Delta\rho_0}{\rho_{ref}}$

where ρ_1 is a measure of the magnitude of $\delta\rho(x,y,z)$ and $\Delta\rho_0$ is the change in ρ_0 over a depth h.

Setting $(D/Dt \rightarrow (U/L)(D'/Dt'))$ etc, where $'$ indicate non-dimensional parameters, Eqs. (18)–(21) become:

$$\frac{D'\mathbf{v}'_h}{Dt'} + \left(\frac{P_{hy}}{U^2}\right)\nabla'_h(p'_s + p'_{hy} + np'_{nh}) + \left(\frac{FL}{U}\right)f'\boldsymbol{k} \times\mathbf{v}'_\mathbf{h} = 0 \tag{23}$$

$$\frac{D'w'}{Dt'} + n\left(\frac{P_{nh}}{U^2}\right)\left(\frac{L}{h}\right)\left(\frac{U}{W}\right)\frac{\partial p'_{nh}}{\partial z'} = 0 \tag{24}$$

$$\frac{D'b'}{Dt'} + \left(\frac{\Delta\rho_0}{\rho_1}\right)\left(\frac{L}{h}\right)\left(\frac{W}{U}\right)N'^2 w' = 0 \tag{25}$$

$$\Delta'_h\cdot\mathbf{v}'_\mathbf{h} + \left(\frac{W}{U}\right)\left(\frac{L}{h}\right)\frac{\partial w'}{\partial z'} = 0 \tag{26}$$

where:

$$n = \frac{P_{nh}}{P_{hy}}$$

is the non-hydrostatic parameter.

Now let us suppose that the flow is 'close' to geostrophic and hydrostatic balance:

geostrophic

$$\frac{P_{hy}}{U^2} = \frac{FL}{U} = \frac{1}{R_o} \tag{27}$$

hydrostatic

$$P_{\mathrm{hy}} = \frac{\rho_1 gh}{\rho_{\mathrm{ref}}} \tag{28}$$

Continuity (26) together with geostrophy implies that:

$$\frac{W}{U}\frac{L}{h} \simeq R_{\mathrm{o}} \tag{29}$$

and since $(D'/Dt)b' \simeq N'^2 w' \simeq 1$, Eq. (25) implies that:

$$\frac{W}{U}\frac{L}{h} \simeq \frac{\rho_1}{\Delta\rho_0} \tag{30}$$

Combining Eqs. (27)–(30), we deduce that:

$$R_{\mathrm{i}} R_{\mathrm{o}}^2 \simeq 1 \tag{31}$$

where R_{i} is the Richardson number of the flow given by:

$$R_{\mathrm{i}} = \frac{N^2 h^2}{U^2} = \frac{g\Delta\rho_0 h}{\rho_{\mathrm{ref}} U^2} = \frac{c^2}{U^2} \tag{32}$$

where c is the speed of internal gravity waves.

The result (31) is well known and *defines* the quasi-geostrophic regime; if the R_{i} of the large-scale flow is large, then the R_{o} is small and the flow quasi-geostrophic.

We may now write the set Eqs. (23)–(26) in terms of R_{i}, R_{o} and $\gamma = h/L$, the aspect ratio of the motion thus:

$$R_0 \frac{D'\mathbf{v}'_{\mathrm{h}}}{Dt'} + (\nabla'_{\mathrm{h}}(p'_{\mathrm{s}} + p'_{\mathrm{hy}} + nqp'_{\mathrm{nh}}) + f'\boldsymbol{k}\times\mathbf{v}'_{\mathbf{h}} = 0 \tag{33}$$

$$\frac{D'w'}{Dt'} + \frac{\partial p'_{\mathrm{nh}}}{\partial z'} = 0 \tag{34}$$

$$\frac{D'b'}{Dt'} + N'^2 w' = 0 \tag{35}$$

$$R_{\mathrm{o}} \frac{\partial w'}{\partial z'} + \nabla'_{\mathrm{h}} \cdot \mathbf{v}'_{\mathbf{h}} = 0 \tag{36}$$

where:

$$n = \frac{\gamma^2}{R_{\mathrm{i}}}$$

is the non-hydrostatic parameter derived in Section 2.1.

References

Adcroft, A., Hill, C.N., Marshall, J.C., 1997. Representation of Topography by Shaved Cells in a Height Coordinate Ocean Model. Month. Weath. Rev. 125, 2293–2315.

Brasseur, P., Beckers, J.M., Brankart, J.M., Schoenauen, 1996. Seasonal temperature and salinity fields in the Mediterranean Sea: climatological analyses of an historical data set. Deep Sea Res. 43, 159–192.

Browning, G.L., Holland, W.R., Kreiss, H.-O., Worley, S.J., 1990. An accurate hyperbolic system for approximately hydrostatic and incompressible flows. Dyn. Atmos. Oceans 14, 303–332.

Brugge, R., Jones, H.L., Marshall, J.C., 1991. Non-hydrostatic ocean modeling for studies of open-ocean deep convection. Elsevier Oceanography Series, pp. 325–340.

Bryan, K., 1969. A numerical model for the study of the circulation of the world ocean. J. Comp. Phys. 4, 347–376.

Coates, M.J., Ivey, G.V., Taylor, J.R., 1995. Unsteady, turbulent convection in to a rotating linearly stratified fluid: modeling deep ocean convection. J. Phys. Oceanogr. 25, 3032–3050.

Deardorff, J.W., Willis, G.E., 1967. Investigation of turbulent, thermal convection between horizontal plates. J. Fluid Mech. 28, 675–704.

Denbo, D.W., Skyllingstad, E.D., 1994. An ocean large eddy model with application to deep convection in the Greenland Sea. J. Geophys. Res.

Ducowicz, J.K., Smith, R.D., Malone, R.C., 1993. A reformulation and implementation of the Bryan–Cox–Semtner ocean model on the connection machine. J. Atmos. Oceanic Tech. 10, 195–208.

Emanuel, K., 1994. Atmospheric convection. Oxford Univ. Press, p. 580.

Garwood, Isakari, Gallacher, 1994. Thermobaric convection, In AGU Monograph for Nansen Centennial.

Haine, T.W.N., Marshall, J.C., 1998. Gravitational, symmetric and baroclinic instability of the ocean mixed layer. J. Phys. Oceanogr. 28, 634–658.

Harlow, F.H., Welch, J.E., 1965. Time dependent viscous flow. Phys. Fluids 8, 2182–2193.

Hill, C.N., Marshall, J.C., 1995. Application of a parallel Navier Stokes model to ocean circulation Parallel Computational Fluid Dynamics: Implementations and Results Using Parallel Computers. Elsevier, Holland, pp. 545–552.

Hill, C.N., Shaw, A., 1996. Transitioning from MPP to SMP: Experiences with a Navier Stokes solver. Proceedings of the Seventh European Centre for Medium Range Weather Forecasting (ECMWF) Workshop on the Use of Parallel Processors in Meteorology, December 1996.

Jones, H.L., Marshall, J.C., 1993. Convection with rotation in a neutral ocean: a study of open-ocean deep convection. J. Phys. Oceanogr. 23, 1009–1039.

Julien, K., Legg, S., McWilliams, J., Werne, J., 1996. Rapidly rotating turbulent Raleigh–Benard convection. J. Fluid. Mech. 322, 234–273.

Kerr, R.M., Herring, J.R., Brandenburg, A., 1995. Large-scale structure in Rayleigh–Benard convection with impenetrable sidewalls. Chaos Solitons Fractals 5, 2047.

Legg, S.A., Jones, H.L., Visbeck, M., 1996. The role of baroclinic instability in open ocean deep convection: a heton perspective. J. Phys. Oceanogr. 26, 2251–2266.

Legg, S.A., Marshall, J.C., 1993. A heton model of open ocean convection. J. Phys. Oceanogr. 23, 1040–1056.

Marshall, J.C., Schott, F., in press. Open-ocean convection; Observations, theory and models. Rev. Geophys. in press.

Marshall, J.C., Hill, C.N., Perelman, L., Adcroft, A., 1997a. Hydrostatic, quasi-hydrostatic and non-hydrostatic ocean-modeling. J. Geophys. Res. 102 (C3), 5733–5752.

Marshall, J.C., Adcroft, A., Hill, C.N., Perelman, L., Heisey, C., 1997b. A finite-volume, incompressible Navier Stokes model for studies of the ocean on parallel computers. J. Geophys. Res. 102 (C3), 5753–5766.

Marshall, J.C., Whitehead, J.A., Yates, T., 1994. Laboratory and numerical experiments in oceanic convection. In: Malanotte-Rizzoli, Robinson (Eds.), Ocean Processes in Climate Dynamics: Global and Mediterranean Examples, Kleuver Academic Publishers, p. 437.

Mason, P.J., 1994. Large eddy simulation: a critical review of technique. Q. J. R. Meteorol. Soc. 120, 1.

Maxworthy, T., Narimousa, S., 1994. Unsteady, turbulent convection in to a homogeneous, rotating fluid, with oceanographic applications. J. Phys. Oceanogr. 24, 865–887.

Menemenlis, D., Webb, T., Wunsch, C., Send, U., Hill, C., 1997. Basin-scale ocean circulation from combined altimetric, tomographic and model data. Nature 385, 618–621.

Miller, M.J., 1974. On the use of pressure as a vertical coordinate in modeling convection. Q. J. R. Meteorol. Soc. 100, 155–162.

Sander, J., Wolf-Gladrow, D., Olbers, D., 1995. Numerical studies of open-ocean deep convection. J. Geophys. Res. 100 (C10), 20579–20600.

Send et al., 1977.

Shaw, A., Arvind, Cho, K., Hill, C., Johnson, R.-P., Marshall, J.C., 1998. A comparison of implicitly parallel multi-threaded and data-parallel implementations of an ocean model based on the Navier Stokes equations. J. Parallel Distributed Computing 48 (1), 1–51.

Visbeck, M., Marshall, J.C., Jones, H.L., 1996. On the dynamics of convective 'chimneys' in the ocean. J. Phys. Oceanogr. 26, 1721–1734.

Whitehead, J., Marshall, J.C., Hufford, G., 1996. Convection in a rotating, stratified fluid. J. Geophys. Res. 101 (C10), 25705–25721.